THE JOURNAL OF PHYSICAL CHEMISTRY LETTERS
A JOURNAL OF THE AMERICAN CHEMICAL SOCIETY

pubs.acs.org/JPCL

Letter

Tunable Polarized Microcavity Characterized by Magnetic Circular Dichroism Spectrum

Dingwei Chen, Zhiyuan Zhao, Nai Jiang, Hui Zhu, Shuai Zhao, Pingheng Tan, Dahai Wei, Houzhi Zheng, and Chao Shen*

Cite This: J. Phys. Chem. Lett. 2022, 13, 3244–3250

Read Online

ACCESS | Metrics & More | Article Recommendations

ABSTRACT: Tunable resonator is a powerful building block in fields like color filtering and optical sensing. The control of its polarization characteristics can significantly expand the applications. Nevertheless, the methods for resonator dynamic tuning are limited. Here, a magnetically regulated circular polarized resonant microcavity is demonstrated with an ultrathin ferrimagnetic composite metal layer Ta/CoTb. We successfully tuned the cavity resonant frequency and polarization performance. A huge magnetic circular dichroism (MCD) signal (~3.41%) is observed, and the microcavity valley position shifts 5.41 nm when a small magnetic field is applied. This resonant cavity has two-stable states at 0 T due to the magnetic remanence of CoTb film and can be switched using a tiny magnetic field (~0.01 T). Our result shows that the ferrimagnetic film-based tunable microcavity can be a highly promising candidate for on-chip magneto-optical (MO) devices.

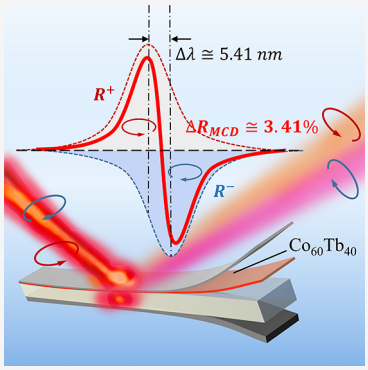

Generating colors or images via on-chip resonant cavity and other micro/nano-structures has attracted plenty of research interest within the past decades.[1−3] These well-designed structures, including nanoapertures arrays,[4] metallic plasmonic arrays,[5−9] nanodisk arrays,[10−12] asymmetric Fabry−Pérot cavities,[1,13] dielectric gratings,[14] and electrochromic polymer films,[15,16] have been proved to be facile and feasible in the fields of imaging, printing, and color filtering. Among them, the Fabry−Pérot microcavity structure, realized with asymmetrical metals and dielectrics, has drawn considerable attention due to its low optical loss, high surface quality, ease of preparation and cost-effectiveness. For instance, a metal−insulator−metal (MIM) color filter was reported with a high transmittance peak intensity of 60% and a narrow bandwidth of ~40 nm,[1] providing a new promise for on-chip color filtering. Furthermore, the dynamic control has partly been achieved in a Fabry−Pérot microcavity structure by adjusting external conditions such as pH, alcohol concentration,[17] and temperature.[18] And the dynamic control may be used in advanced functionalities like sensing and monitoring. However, the real-time regulation as well as the initial state recovery still are two main challenges for the applications of dynamic controlling.

Meanwhile, specific architectures with polarization-dependent response are in great need for future information encryption,[19] optical anticounterfeiting[18] and other applications.[20−22] Research on the magneto-optical (MO) effect has been one of the main topics studied,[23,24] and large MO responses can further be used in dynamic regulation, magnetic information storage, magnetic field detection, etc.[24−29] A series of attempts have been made to design and fabricate the magnetic field-controllable microstructure, which is non-destructive, recoverable, and real-time corresponsive. For example, with yttrium iron garnet microspheres, the MO coupling, i.e., polarization rotation via the Faraday effect, was verified, and therefore a 20 pm resonant peak shift was demonstrated.[30] In another work, the Kerr amplitude was amplified in a microcavity,[31] and the linkage between the modes of microcavity and the magnetism of material is further confirmed by MO Kerr tests in a MIM resonator.[32] Nevertheless, the mechanism of generating large MO signals has not been fully studied in a resonant microstructure. Magnetic circular dichroism (MCD), as an important MO effect, has a great ability to intrinsically explore the nexus between microstructure and MO properties.[33] For example, the *g*-factor of Mn^{2+}-doped $(CdSe)_{13}$ clusters has been calculated, and it has promoted the understanding of MCD properties of doped semiconductors in a quantum nanostructure.[34] Different MCD signals have been demonstrated in different gold nanorod structures, which pave a new way to achieve tunable MO response in an optical microstructure.[35]

Received: February 26, 2022
Accepted: March 31, 2022
Published: April 6, 2022

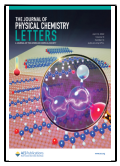

https://doi.org/10.1021/acs.jpclett.2c00594
J. Phys. Chem. Lett. 2022, 13, 3244−3250

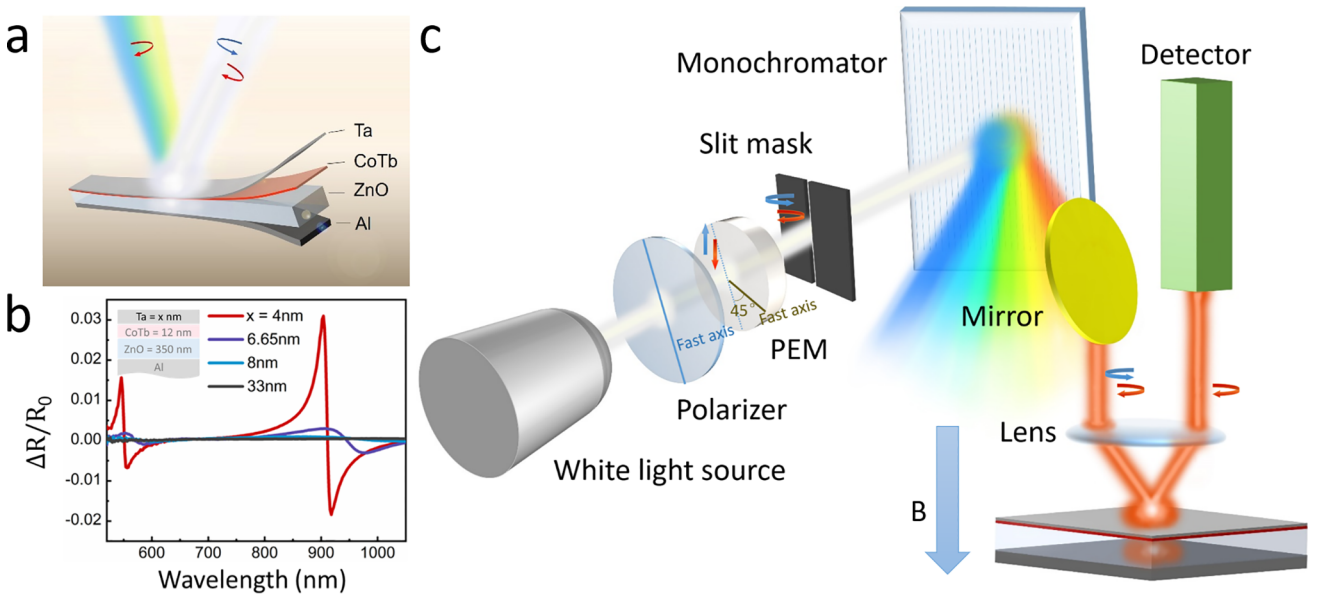

Figure 1. (a) Schematic illustration for the magnetic MIM resonant microcavity. (b) MCD spectra for the microcavities with different thicknesses of the Ta metal layer. (c) Schematic diagram for the MO testing configuration.

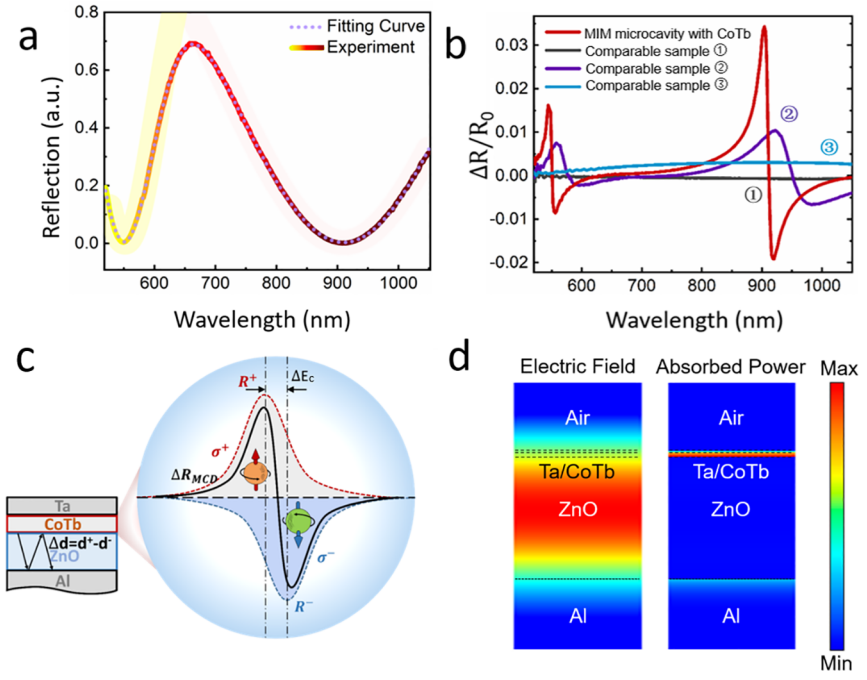

Figure 2. (a) Reflectance and (b) MCD spectra (red line, B = 1 T) for the magnetic MIM microcavity. ①, ②, and ③ are comparative samples, respectively. ① is for the comparation between with and without magnetic layer. Its structure is 16 nm Ta/ZnO/Al. ② is for the microcavity with or without an intercalation layer. Its structure is 2 nm Ta/12 nm CoTb/2 nm Ta/ZnO/Al. ③ is for CoTb with and without microcavity structure. Its structure is 4 nm Ta/12 nm CoTb/SiO_2/Si substrate. (c) Schematic diagram for the MCD origin. (d) Simulated light field distribution and absorption loss results of the as-proposed structure.

Herein, we report a magnetic dynamic regulation of resonant valley position utilizing an asymmetric MIM interference microcavity, and the top layer is made of ultrathin artificial ferrimagnetic multilayer composite Ta/CoTb film. A significant MCD signal reaches up to ∼3.41% when an external magnetic field of 1 T is applied. The MCD signals are proportional to the spectral difference of left and right-handed circularly polarized light (LCP and RCP) at different wavelengths. Since the light is reflected back and forth in the resonant microcavity, the MCD signal is amplified by a factor of nearly 10 compared to pure CoTb material. We further investigate the origination of the large MCD signal and match the valley position shift of MIM microstructure with ferrimagnetic material properties of CoTb material.

METHODS

MIM resonant microcavity consists of two reflective metal end faces and a transparent dielectric layer in between. We modified the conventional structure by replacing the non-magnetic upper reflector with an ultrathin ferrimagnetic Ta/

https://doi.org/10.1021/acs.jpclett.2c00594
J. Phys. Chem. Lett. 2022, 13, 3244−3250

Table 1. Valley Position, FWHM, and ΔE_c with External Magnetic Field of Different Samples

component of sample	valley position (nm)	FWHM (nm)	ΔE_c (meV)
4 nm Ta/12 nm $Co_{60}Tb_{40}$/350 nm ZnO/150 nm Al	908	284	8.14 (1T)
	548	104	3.78 (1T)
2 nm Ta/12 nm $Co_{60}Tb_{40}$/2 nm Ta/350 nm ZnO/150 nm Al	936	256	2.20 (1T)
	568	170	2.25 (1T)
4 nm Ta/12 nm $Co_{60}Tb_{40}$/510 nm ZnO/150 nm Al	810	260	11.62 (1T)
4 nm Ta/12 nm $Co_{70}Tb_{30}$/510 nm ZnO/150 nm Al	790	263	2.86 (1T)

CoTb metal film, as shown in Figure 1a. The optical interference medium layer, composed of oriented and transparent polycrystalline zinc oxide (ZnO), was grown using DC magnetron sputtering on a ∼150 nm Al substratum. After that, the CoTb layer was deposited using codeposition magnetron sputtering under a base pressure of 2×10^{-8} Torr. Besides this, a Ta metal film was sputtered on the top surface as an oxidation-preventing layer and magnetism-inducing layer.[36,37] We tested the MCD characteristics of samples with different thicknesses of Ta metal film, which retain a determinate thickness to ensure long-term oxidation resistance, as shown in Figure 1b. Under the premise of preventing oxidation and magnifying the MCD spectrum signal, the thickness of the Ta layer was chosen as ∼4 nm. The MCD and reflection properties of samples were characterized via a home-built MCD measurement setup. The monochromatic incident light was generated by a supercontinuum white light source, separated by a monochromator, and modulated into LCP and RCP via a linear polarizer and photoelastic modulator (PEM). The spectra range varied from 550 to 1050 nm, and the light spot size was ∼1 μm. At the same time, a magnetic field parallel to the incident light was applied. The schematic diagram of the measurement system is illustrated in Figure 1c.

The resonant valleys of the sample are at ∼548 and ∼908 nm (shown in the gradient color line of Figure 2a). The valley positions and the full width half-maximum (FWHM) (shown in Table 1) are obtained by the Gaussian fitting. Among them, the ∼548 nm resonance valley is in a higher-order mode, which appears in visible wavelength when the intermediate dielectric layer ZnO gets thicker.[1] For an individual semiconductor material, having an exciton absorption peak with smaller FWHM tends to gain a larger MCD signal. The MCD signal can be expressed as $\Delta R_{MCD} \cong -\frac{R_0}{\sqrt{e}\,w}\Delta E$,[38] where the spectral line width w can be defined as $2w = \mathrm{FWHM}/\sqrt{\ln 4}$.[38] The reflection signal and the energy splitting are represented as R_0 and ΔE respectively. We conjectured that it would be the same in the microcavity structure. In the MIM resonant microcavity, the bandwidth is related to the thickness of the upper metal layer. In comparison with the traditional Fabry−Pérot cavity, a cavity with thinner upper metal would lead to broader bandwidth owing to the weaker confinement.[1] However, if the upper metal is too thick, the incident light would be directly reflected by the upper metal layer without reaching the resonator. Therefore, we adjusted the thickness of the upper metal by considering narrowing bandwidth and enlarging the reflection valley signal of the resonator.

The separate 4 nm Ta/12 nm CoTb metal layer on silicon produces a monotonously upward MCD signal as large as ∼0.0025 with a 1 T external magnetic field (blue line in Figure 2b). As the time symmetry is broken under the external magnetic field, the energy band of spin-up electrons and spin-down electrons split, and the refractive indices of LCP and RCP are different at the same wavelength, bringing about the difference reflection spectrum between LCP and RCP. However, the spectrum would not form typical MCD signal going through the zero point, as there is no characteristic absorption valley across the entire visible wavelength for the ferrimagnetic metal CoTb.

In our magnetic resonant microcavity structure, an extremely huge MCD signal as large as ∼0.03 in 902 nm with the same external magnetic field is achieved, as depicted in the red line in Figure 2b. It is worth mentioning that the MCD signal is surprisingly enlarged by more than 10 times. As can be seen, the wavelength position of the middle zero value between the positive peak and negative valley is corresponding to the absorption resonance valley position. The MCD signal is directly dependent on the absorption curve of LCP and RCP. When the absorption valleys of LCP and RCP shift, the MCD spectrum would be an antisymmetrical shape shown in Figure 2c, presenting like the derivative of absorption valley. The distance between the negative valley and positive peak as well as the magnitude of signal in MCD spectrum is related to the valley shift of LCP and RCP. The energy difference between these two resonant valleys is defined as ΔE_C, which is similar to the energy splitting ΔE of the energy band under an external magnetic field in a semiconductor material. We calculated the ΔE_C of valleys in ∼548 and ∼908 nm through the formula mentioned before, the results are shown in Table 1, and the ΔE_C in ∼908 nm is much bigger than that in ∼548 nm. This probably results from the different equivalent refractive index of LCP and RCP in ∼908 nm being bigger than that in ∼548 nm for metal CoTb. Therefore, the MCD signal in ∼908 nm is much larger than that in ∼548 nm, though the resonant valley is wider. In a resonant cavity structure, the resonant valley corresponds to the mode of resonant cavity, and therefore the emergence of MCD spectroscopy signifies that the mode of resonant cavity shifts. Specifically, as light is repeatedly reflected between the top metal layer and bottom metal layer, light with specific wavelengths is resonated and enhanced, producing a resonance valley. There is an equivalent optical path difference of the structure Δd (Δd is defined as $\Delta d = d^+ - d^-$. Among them, d^+ represents the optical path of LCP, while d^- represents the optical path of RCP) caused by the different refractive indices of magnetic material CoTb for LCP and RCP.

For the sake of confirming the origin of the energy splitting of microcavity, we added a 2 nm metal Ta intercalation layer between CoTb layer and ZnO layer and thinned the upper oxidation protection layer metal Ta to 2 nm to keep the total thickness of the upper compound metal layer unchanged. An MCD signal is generated at wavelengths of ∼936 and ∼568 nm. Although the signals are reduced and the FWHM are enlarged, their peak and valley structures still exist as shown in the purple line of Figure 2b. Therefore, it can be considered that the generation of the MO signal has nothing to do with

https://doi.org/10.1021/acs.jpclett.2c00594
J. Phys. Chem. Lett. 2022, 13, 3244−3250

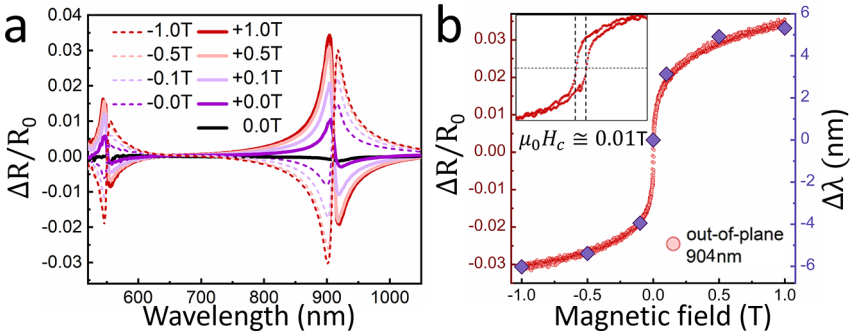

Figure 3. (a) External magnetic field-dependent MCD spectra (where 0T refers to the zero field before magnetization, −0T refers to the magnetic field rising from the negative field to the zero field, and +0T refers to the magnetic field falling from the positive field to the zero field). (b) Calculated wavelength valley shifts as a function of magnetic field intensity and the room-temperature magnetic hysteresis loop for the MCD device under a 904-nm-light illumination with an out-of-plane magnetic field. The inset presents an enlarged hysteresis loop result.

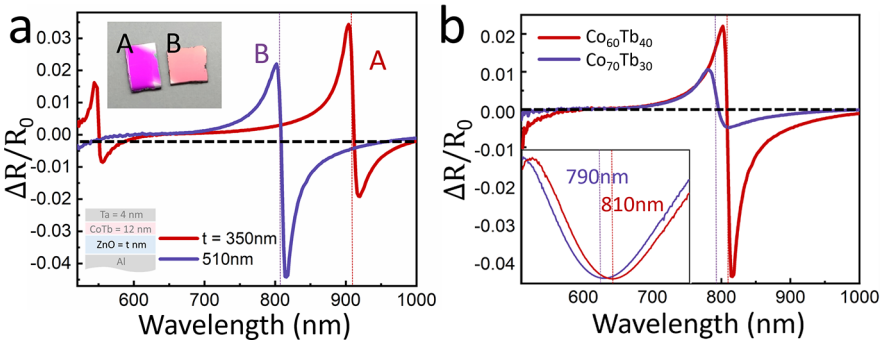

Figure 4. (a) MCD spectra for the resonators with different middle layer thicknesses (B = 1 T). The inset shows the photos for colors of these two samples. (b) MCD spectra for the resonators with different Co components. The inset shows their reflectance spectra.

magnetization of the intermediate layer ZnO, including magnetic Co-doped ZnO caused by the CoTb sputtering process and magnetic proximity effect on ZnO. Also, for the nonmagnetic resonant cavity (black line in Figure 2b), though there are two resonant valleys almost the same as the sample with magnetic upper layer, there is no MCD signal. Therefore, the large MCD signal is derived from the difference in the refractive index of the magnetic material CoTb for LCP and RCP, the principle of which is drawn in Figure 2c.

To better understand the MCD signal mechanism, we simulated and visualized the electric field distribution and absorbed loss, which is shown in Figure 2d. Among them, the simulation is based on the measured birefringence and dichroism of CoTb and ZnO materials by spectroscopic ellipsometry. The light field is mainly distributed in the transparent ZnO layer because most of the light would form a standing wave and be localized in the middle layer in the reflection process between the upper and bottom layers. Since the cavity effect enhances the electric field, there is a great loss in the upper layer. The light would repeatedly reflect back and forth on the upper and bottom metal interfaces, and the upper metal CoTb would absorb the light continually as exhibited in Figure 2d. That is to say, the absorption of the magnetic composite upper layer Ta/CoTb is far larger than that of the normal low-loss media in a MIM resonant cavity, while a conventional cavity would modulate transmission and reflection spectra through effective optical path of quarter wavelength but without absorption involved. Among them, the main absorption comes from the interface between the upper metal layer and the intermediate dielectric ZnO layer, which explains the reason for the decrease of the MCD of the sample with a 2 nm Ta intercalation layer before. Meanwhile, we speculate that the difference in signal size between the positive peak and negative valley in MCD spectroscopy is produced by the different absorption values of LCP and RCP in the CoTb/ZnO intermediate layer.

Furthermore, we tested the MCD spectrum applying different external magnetic fields, and got an almost completely symmetrical MCD spectrum about the positive and negative magnetic fields, as shown in Figure 3a. Besides, we calculated the magnitude of the resonance valley position shift $\Delta\lambda$ under the influence of different external magnetic fields as shown in the purple point of Figure 3b. As displayed in the red line in Figure 3b, we also obtained the magnetic hysteresis loop with an out-of-plane magnetic field using MCD measurement at the wavelength of 904 nm, which is consistent with $\Delta\lambda$ in shape. The coercive force is ∼0.01 T, and the equivalent saturation MCD signal is 0.03. Due to the multidomain flipping,[39] it would feature a rectangular loop with tailings, which is not completely rectangle like conventional ferromagnetic materials. It is worth noting that, when the magnetic field is 0T, there are two stable magnetization states (noted as −0T and +0T state, determined by the magnetization process), which can be switched with a tiny magnetic field. This kind of bistable property originates from the out-of-plane remanence and can be very useful for magnetic storage,[40] polarization encryption. At the same time, as the magnetic field increases, the magnetization of the sample can be continuously controlled as well as the MCD signal, which indicates that it is promising to achieve a dynamic color-changing filter or polarized image display with magnetic field regulation when the device performance is further enhanced in the future.

https://doi.org/10.1021/acs.jpclett.2c00594
J. Phys. Chem. Lett. 2022, 13, 3244−3250

In order to further demonstrate its application prospects, we prepared samples with different thicknesses of the intermediate layer of ZnO, and obtained their MCD spectrum, as shown in Figure 4a. The valley position shifted from ∼908 to 810 nm, as the thickness of the intermediate layer t increased from 350 to 510 nm. The color of samples changed visibly to the naked eye as shown in the illustration of Figure 4a. The MCD signal in ∼810 nm reaches a large value of 4.42%, which means we could magnetically tune the resonant valley position (color) around different wavelengths we chose. It shows the potential for future applications in the full visible spectrum. A huge MCD signal is necessary to truly implement the application of magnetic MIM cavity. We deemed that the magnetization property of the magnetic metal layer is critical to the MCD signal. Hence, we changed the Co_xTb_y composition of the magnetic layer and acquired the MCD spectra, as shown in Figure 4b. The resonant valley positions of the two microcavities with different components are slightly different, which may be due to the inevitable thickness difference from the set value during the preparation process. However, the signal size is much smaller, which indicates that the magnetic response of microcavities is strongly influenced by magnetic materials. Thus, we can modify the MO response by changing the Co_xTb_y components. More detailed studies are needed to reveal the relationship between components and MCD spectrum in the future, which is beyond the scope of this paper. Nevertheless, it undoubtedly shows the potential to control the mode of resonant cavity under different circumstances.

In summary, we designed and demonstrated a magnetically tunable resonant microcavity with a ferrimagnetic CoTb metal upper layer, and systematically investigated its MO properties. A main resonance absorption valley at ∼908 nm is observed, and an MCD signal larger than 3.41% is achieved when the applied magnetic field is 1 T, which is 10 times larger than the signal of CoTb individually. At the same time, the resonant cavity realizes a bistable state under the zero magnetic field, which can be converted by a very small external field (∼0.01 T). It is inferred that the large MCD signal originates from the different reflection properties of magnetic metal top layer for LCP and RCP light, as well as the continuous light reflection at the upper metal interfaces. The CoTb reflection differences for various circularly polarized lights are amplified within the multiple reflection process. Besides this, a direct connection between the resonance valley position shift and the hysteresis loop is observed. The potential tuning capacity of this resonant microcavity is further demonstrated by adjusting the dielectric thickness. Notably, this nondestructive dynamic tuning technique is achieved based on a magnetic microcavity structure with high reversibility and also a high universality in device fabrications, paving a new way for future sensors, multicolor indicators, and information encryption.

AUTHOR INFORMATION

Corresponding Author

Chao Shen − *State Key Laboratory for Superlattices and Microstructures, Institute of Semiconductors, Chinese Academy of Sciences, Beijing 100083, China; Center of Materials Science and Optoelectronics Engineering, University of Chinese Academy of Sciences, Beijing 100049, China;* orcid.org/0000-0002-3664-4874; Email: shenchao@semi.ac.cn

Authors

Dingwei Chen − *State Key Laboratory for Superlattices and Microstructures, Institute of Semiconductors, Chinese Academy of Sciences, Beijing 100083, China; Center of Materials Science and Optoelectronics Engineering, University of Chinese Academy of Sciences, Beijing 100049, China*

Zhiyuan Zhao − *State Key Laboratory for Superlattices and Microstructures, Institute of Semiconductors, Chinese Academy of Sciences, Beijing 100083, China; Center of Materials Science and Optoelectronics Engineering, University of Chinese Academy of Sciences, Beijing 100049, China*

Nai Jiang − *State Key Laboratory for Superlattices and Microstructures, Institute of Semiconductors, Chinese Academy of Sciences, Beijing 100083, China; Center of Materials Science and Optoelectronics Engineering, University of Chinese Academy of Sciences, Beijing 100049, China*

Hui Zhu − *State Key Laboratory for Superlattices and Microstructures, Institute of Semiconductors, Chinese Academy of Sciences, Beijing 100083, China*

Shuai Zhao − *State Key Laboratory for Superlattices and Microstructures, Institute of Semiconductors, Chinese Academy of Sciences, Beijing 100083, China; Center of Materials Science and Optoelectronics Engineering, University of Chinese Academy of Sciences, Beijing 100049, China;* orcid.org/0000-0001-7171-2943

Pingheng Tan − *State Key Laboratory for Superlattices and Microstructures, Institute of Semiconductors, Chinese Academy of Sciences, Beijing 100083, China; Center of Materials Science and Optoelectronics Engineering, University of Chinese Academy of Sciences, Beijing 100049, China;* orcid.org/0000-0001-6575-1516

Dahai Wei − *State Key Laboratory for Superlattices and Microstructures, Institute of Semiconductors, Chinese Academy of Sciences, Beijing 100083, China; Center of Materials Science and Optoelectronics Engineering, University of Chinese Academy of Sciences, Beijing 100049, China*

Houzhi Zheng − *State Key Laboratory for Superlattices and Microstructures, Institute of Semiconductors, Chinese Academy of Sciences, Beijing 100083, China; Center of Materials Science and Optoelectronics Engineering, University of Chinese Academy of Sciences, Beijing 100049, China*

Complete contact information is available at: https://pubs.acs.org/10.1021/acs.jpclett.2c00594

Notes

The authors declare no competing financial interest.

ACKNOWLEDGMENTS

We thank Prof. Tianrui Zhai and Prof. Xiaoyu Shi (Beijing University of Technology) for valuable discussion. C.S. acknowledges the support from the Youth Innovation Promotion Association, Chinese Academy of Sciences (2019114), and the Strategic Priority Research Program of the Chinese Academy of Sciences (XDB30000000).

REFERENCES

(1) Li, Z.; Butun, S.; Aydin, K. Large-Area, Lithography-Free Super Absorbers and Color Filters at Visible Frequencies Using Ultrathin Metallic Films. *ACS Photonics* **2015**, *2*, 183−188.

(2) Kristensen, A.; Yang, J. K. W.; Bozhevolnyi, S. I.; Link, S.; Nordlander, P.; Halas, N. J.; Mortensen, N. A. Plasmonic Colour Generation. *Nat. Rev. Mater.* **2017**, *2*, 16088.

(3) Kumar, K.; Duan, H.; Hegde, R. S.; Koh, S. C. W.; Wei, J. N.; Yang, J. K. W. Printing Colour at the Optical Diffraction Limit. *Nat. Nanotechnol.* **2012**, *7*, 557−561.
(4) Li, Z.; Clark, A. W.; Cooper, J. M. Dual Color Plasmonic Pixels Create a Polarization Controlled Nano Color Palette. *ACS Nano* **2016**, *10*, 492−498.
(5) Tseng, M. L.; Yang, J.; Semmlinger, M.; Zhang, C.; Nordlander, P.; Halas, N. J. Two-Dimensional Active Tuning of an Aluminum Plasmonic Array for Full-Spectrum Response. *Nano Lett.* **2017**, *17*, 6034−6039.
(6) Peng, J. L.; Jeong, H. H.; Lin, Q. Q.; Cormier, S.; Liang, H. L.; De Volder, M. F. L.; Vignolini, S.; Baumberg, J. J. Scalable Electrochromic Nanopixels Using Plasmonics. *Sci. Adv.* **2019**, *5*, eaaw2205.
(7) Duan, X.; Kamin, S.; Liu, N. Dynamic Plasmonic Colour Display. *Nat. Commun.* **2017**, *8*, 14606.
(8) Olson, J.; Manjavacas, A.; Basu, T.; Huang, D.; Schlather, A. E.; Zheng, B.; Halas, N. J.; Nordlander, P.; Link, S. High Chromaticity Aluminum Plasmonic Pixels for Active Liquid Crystal Displays. *ACS Nano* **2016**, *10*, 1108−1117.
(9) Zhang, Y.; Liu, Q.; Mundoor, H.; Yuan, Y.; Smalyukh, I. I. Metal Nanoparticle Dispersion, Alignment, and Assembly in Nematic Liquid Crystals for Applications in Switchable Plasmonic Color Filters and E-Polarizers. *ACS Nano* **2015**, *9*, 3097−3108.
(10) Sun, S.; Yang, W.; Zhang, C.; Jing, J.; Gao, Y.; Yu, X.; Song, Q.; Xiao, S. Real-Time Tunable Colors from Microfluidic Reconfigurable All-Dielectric Metasurfaces. *ACS Nano* **2018**, *12*, 2151−2159.
(11) Yang, W.; Xiao, S.; Song, Q.; Liu, Y.; Wu, Y.; Wang, S.; Yu, J.; Han, J.; Tsai, D.-P. All-Dielectric Metasurface for High-Performance Structural Color. *Nat. Commun.* **2020**, *11*, 1864.
(12) Proust, J.; Bedu, F.; Gallas, B.; Ozerov, I.; Bonod, N. All-Dielectric Colored Metasurfaces with Silicon Mie Resonators. *ACS Nano* **2016**, *10*, 7761−7767.
(13) Kim, T.; Yu, E.-S.; Bae, Y.-G.; Lee, J.; Kim, I. S.; Chung, S.; Lee, S.-Y.; Ryu, Y.-S. Asymmetric Optical Camouflage: Tuneable Reflective Colour Accompanied by the Optical Janus Effect. *Light Sci. Appl.* **2020**, *9*, 175.
(14) Wang, W.; Guan, Z.; Xu, H. A High Speed Electrically Switching Reflective Structural Color Display with Large Color Gamut. *Nanoscale* **2021**, *13*, 1164−1171.
(15) Zhang, Q.; Tsai, C.-Y.; Li, L.-J.; Liaw, D.-J. Colorless-to-Colorful Switching Electrochromic Polyimides with Very High Contrast Ratio. *Nat. Commun.* **2019**, *10*, 1239.
(16) Zheng, R.; Wang, Y.; Jia, C.; Wan, Z.; Luo, J.; Malik, H. A.; Weng, X.; Xie, J.; Deng, L. Intelligent Biomimetic Chameleon Skin with Excellent Self-Healing and Electrochromic Properties. *ACS Appl. Mater. Interfaces* **2018**, *10*, 35533−35538.
(17) Kwon, H.; Kim, S. Chemically Tunable, Biocompatible, and Cost-Effective Metal-Insulator-Metal Resonators Using Silk Protein and Ultrathin Silver Films. *ACS Photonics* **2015**, *2*, 1675−1680.
(18) Chen, D.; Wang, T.; Song, G.; Du, Y.; Lv, J.; Zhang, X.; Li, Y.; Zhang, L.; Hu, J.; Fu, Y.; et al. Dynamic Tunable Color Display Based on Metal-Insulator-Metal Resonator with Polymer Brush Insulator Layer as Signal Transducer. *ACS Appl. Mater. Interfaces* **2019**, *11*, 41668−41675.
(19) Ren, S.; Liu, C.; Xu, K.; Jiang, N.; Hu, F.; Tan, P.-H.; Zheng, H.; Xu, X.; Shen, C.; Zhang, J. Azimuth-Resolved Circular Dichroism of Metamaterials. *J. Phys. Chem. Lett.* **2022**, *13*, 1697−1704.
(20) Chen, W.; Zhang, S.; Zhou, M.; Zhao, T.; Qin, X.; Liu, X.; Liu, M.; Duan, P. Two-Photon Absorption-Based Upconverted Circularly Polarized Luminescence Generated in Chiral Perovskite Nanocrystals. *J. Phys. Chem. Lett.* **2019**, *10*, 3290−3295.
(21) Li, L.; Jin, L.; Zhou, Y.; Li, J.; Ma, J.; Wang, S.; Li, W.; Li, D. Filterless Polarization-Sensitive 2D Perovskite Narrowband Photodetectors. *Adv. Opt. Mater.* **2019**, *7*, 1900988.
(22) Zhao, W.; Su, R.; Huang, Y.; Wu, J.; Fong, C. F.; Feng, J.; Xiong, Q. Transient Circular Dichroism and Exciton Spin Dynamics in All-Inorganic Halide Perovskites. *Nat. Commun.* **2020**, *11*, 5665.
(23) Long, G.; Jiang, C.; Sabatini, R.; Yang, Z.; Wei, M.; Quan, L. N.; Liang, Q.; Rasmita, A.; Askerka, M.; Walters, G.; et al. Spin Control in Reduced-Dimensional Chiral Perovskites. *Nat. Photonics* **2018**, *12*, 528−533.
(24) Yin, T.; Ulman, K. A.; Liu, S.; Granados del Águila, A.; Huang, Y.; Zhang, L.; Serra, M.; Sedmidubsky, D.; Sofer, Z.; Quek, S. Y.; et al. Chiral Phonons and Giant Magneto-Optical Effect in $CrBr_3$ 2D Magnet. *Adv. Mater.* **2021**, *33*, 2101618.
(25) Betzig, E.; Trautman, J. K.; Wolfe, R.; Gyorgy, E. M.; Finn, P. L.; Kryder, M. H.; Chang, C. H. Near-Field Magneto-Optics and High Density Data Storage. *Appl. Phys. Lett.* **1992**, *61*, 142−144.
(26) Vanwolleghem, M.; Van Parys, W.; Van Thourhout, D.; Baets, R.; Lelarge, F.; Gauthier-Lafaye, O.; Thedrez, B.; Wirix-Speetjens, R.; Lagae, L. Experimental Demonstration of Nonreciprocal Amplified Spontaneous Emission in a CoFe Clad Semiconductor Optical Amplifier for Use as an Integrated Optical Isolator. *Appl. Phys. Lett.* **2004**, *85*, 3980−3982.
(27) Temnov, V. V.; Armelles, G.; Woggon, U.; Guzatov, D.; Cebollada, A.; Garcia-Martin, A.; Garcia-Martin, J.-M.; Thomay, T.; Leitenstorfer, A.; Bratschitsch, R. Active Magneto-Plasmonics in Hybrid Metal-Ferromagnet Structures. *Nat. Photonics* **2010**, *4*, 107−111.
(28) Nakamura, T.; Tani, S.; Ito, I.; Kobayashi, Y. Magneto-Optic Modulator for High Bandwidth Cavity Length Stabilization. *Opt. Express* **2017**, *25*, 4994−5000.
(29) Sepúlveda, B.; Calle, A.; Lechuga, L. M.; Armelles, G. Highly Sensitive Detection of Biomolecules with the Magneto-Optic Surface-Plasmon-Resonance Sensor. *Opt. Lett.* **2006**, *31*, 1085−1087.
(30) Haigh, J. A.; Langenfeld, S.; Lambert, N. J.; Baumberg, J. J.; Ramsay, A. J.; Nunnenkamp, A.; Ferguson, A. J. Magneto-Optical Coupling in Whispering-Gallery-Mode Resonators. *Phys. Rev. A* **2015**, *92*, 063845.
(31) Kim, D.; Oh, Y.-W.; Kim, J. U.; Lee, S.; Baucour, A.; Shin, J.; Kim, K.-J.; Park, B.-G.; Seo, M.-K. Extreme Anti-Reflection Enhanced Magneto-Optic Kerr Effect Microscopy. *Nat. Commun.* **2020**, *11*, 5937.
(32) Yamane, H.; Yasukawa, Y.; Kobayashi, M. Polar Kerr Effect and Perpendicular Magnetic Anisotropy in Fabry-Pérot Cavity Containing CoPt/AZO Magneto-Optical Interference Layer. *J. Appl. Phys.* **2021**, *129*, 203902.
(33) Han, B.; Gao, X.; Lv, J.; Tang, Z. Magnetic Circular Dichroism in Nanomaterials: New Opportunity in Understanding and Modulation of Excitonic and Plasmonic Resonances. *Adv. Mater.* **2020**, *32*, 1801491.
(34) Yang, J.; Fainblat, R.; Kwon, S. G.; Muckel, F.; Yu, J. H.; Terlinden, H.; Kim, B. H.; Iavarone, D.; Choi, M. K.; Kim, I. Y.; et al. Route to the Smallest Doped Semiconductor: Mn^{2+}-Doped $(CdSe)_{13}$ Clusters. *J. Am. Chem. Soc.* **2015**, *137*, 12776−12779.
(35) Han, B.; Gao, X.; Shi, L.; Zheng, Y.; Hou, K.; Lv, J.; Guo, J.; Zhang, W.; Tang, Z. Geometry-Modulated Magnetoplasmonic Optical Activity of Au Nanorod-Based Nanostructures. *Nano Lett.* **2017**, *17*, 6083−6089.
(36) Avci, C. O.; Garello, K.; Mendil, J.; Ghosh, A.; Blasakis, N.; Gabureac, M.; Trassin, M.; Fiebig, M.; Gambardella, P. Magneto-resistance of Heavy and Light Metal/Ferromagnet Bilayers. *Appl. Phys. Lett.* **2015**, *107*, 192405.
(37) Kim, J.; Sinha, J.; Hayashi, M.; Yamanouchi, M.; Fukami, S.; Suzuki, T.; Mitani, S.; Ohno, H. Layer Thickness Dependence of the Current-Induced Effective Field Vector in Ta|CoFeB|MgO. *Nat. Mater.* **2013**, *12*, 240−245.
(38) Wu, Y. J.; Shen, C.; Tan, Q. H.; Shi, J.; Liu, X. F.; Wu, Z. H.; Zhang, J.; Tan, P. H.; Zheng, H. Z. Valley Zeeman Splitting of Monolayer MoS_2 Probed by Low-Field Magnetic Circular Dichroism Spectroscopy at Room Temperature. *Appl. Phys. Lett.* **2018**, *112*, 153105.
(39) Yu, J.; Liu, L.; Deng, J.; Zhou, C.; Liu, H.; Poh, F.; Chen, J. Topological Hall Effect in Ferrimagnetic CoTb Single Layer. *J. Magn. Magn. Mater.* **2019**, *487*, 165316.

https://doi.org/10.1021/acs.jpclett.2c00594
J. Phys. Chem. Lett. 2022, 13, 3244−3250

(40) Tannous, C.; Gieraltowski, J. The Stoner-Wohlfarth Model of Ferromagnetism. *Eur. J. Phys.* **2008**, *29*, 475−487.

https://doi.org/10.1021/acs.jpclett.2c00594
J. Phys. Chem. Lett. 2022, 13, 3244−3250